THE JOURNAL OF PHYSICAL CHEMISTRY C

Article

Cite This: J. Phys. Chem. C 2019, 123, 11063−11072

pubs.acs.org/JPCC

Organic Light-Emitting Transistors Based on Pentacene and 4,5-Di(9*H*-carbazol-9-yl)phthalonitrile Doped onto 1,3-Bis(*N*-carbazolyl)benzene

Dae-Kyu Kim, Yoo-Lim Kim, and Jong-Ho Choi*

Department of Chemistry, Research Institute for Natural Sciences, Korea University, 145 Anam-ro, Seongbuk-Gu, Seoul 02841, South Korea

ABSTRACT: In this study, multilayered, organic-based light-emitting transistors (OLETs) were produced and characterized. The neutral cluster beam deposition method was applied to successively deposit organic semiconducting layers of pentacene, 4,5-di(9*H*-carbazol-9-yl)phthalonitrile (2CzPN) doped onto 1,3-bis(*N*-carbazolyl)benzene (mCP), and 1,3,5-tris(1-phenyl-1*H*-benzimidazol-2-yl)benzene (TPBi) as the hole-transport, emissive, and electron-transport layers, respectively. The effects of drain electrodes (Au or Li/Al) and TPBi on the device performance were examined under ambient conditions. The bilayered pentacene (bottom, 50 nm)/mCP:2CzPN (top, 50 nm) and trilayered pentacene (bottom, 50 nm)/mCP:2CzPN (middle, 50 nm)/TPBi (top, 10 nm) OLETs demonstrated both electrical switching functionality and control of electroluminescence (EL) in air. In particular, the EL intensity (I_{EL}) was significantly enhanced in the asymmetric bilayered devices adopting a low work function Li/Al drain electrode owing to the lower electron injection barrier. The operating light emission mechanisms responsible for the observed EL and recombination zone were discussed with the aid of photographic images provided by a charge-coupled device camera.

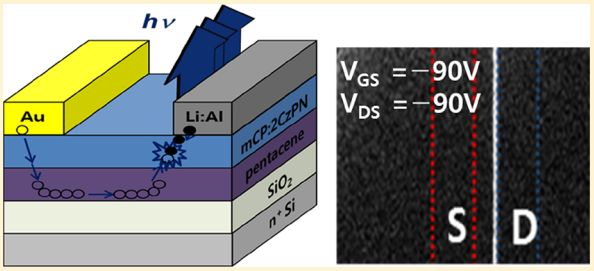

INTRODUCTION

Organic light-emitting transistors (OLETs) have attracted considerable attention for their potential applicability to new organic-based optoelectronic devices.[1−6] OLETs are multifunctional optoelectronic devices that combine the light emission characteristic of organic light-emitting diodes (OLEDs) with the electrical switching property of organic field-effect transistors (OFETs) into a single device.[7−9] An OLET circuit design can be utilized not only to decrease the number of parts required but also to fabricate highly integrated optoelectronic devices through a simple and inexpensive process.[10−12]

The first reported tetracene-based OLETs were operated in the unipolar mode.[1] In the device configuration, however, imbalanced carrier injection and transport existed because of the electron tunneling from the drain electrode to the tetracene active layer. Severe unfavorable exciton quenching at the interface was inevitable. As in OLEDs, facile injection and transport of majority carriers (holes/electrons) are crucial requirements for generating electroluminescence (EL) in OLETs. Different methods to improve carrier injection and transport have been developed. For example, strategies such as interface modification, adopting asymmetric electrodes, and synthesis of new electron-transport materials with high mobility have been reported.[13−17] Efficient injection of both hole and electron carriers has been accomplished using asymmetric electrodes made from low and high work function (WF) metals.[13,14,18,19] Materials such as electron-transporting tris(8-hydroxyquinoline) aluminum (Alq_3), bathophenanthroline, and 1,3,5-tris(1-phenyl-1*H*-benzimi-dazol-2-yl)benzene (TPBi) reduce the potential energy barrier between the emission layer and the injection electrode and also act as a hole-blocking layer at an appropriate energy level compared to the emissive layer, leading to an improvement of the EL performance of the devices.[20,21]

In fabricating OLETs, different schemes have been proposed including single ambipolar materials, co-evaporation of two unipolar materials, and multilayered structures.[22−26] Among the approaches, the majority of the cases of OLETs based on a single component and blending experienced difficulties achieving balanced injection and carrier transport. Although there is growth incompatibility and a physical separation between the transport layers, OLETs adopting bi- or trilayered, heterojunction-based configuration have demonstrated improved carrier injection and transport, resulting in high external quantum efficiency, carrier mobility, and current on/off (I_{on}/I_{off}) ratio.[2,16] This has been well-demonstrated through several studies of multilayer-based OLETs using thiophene and perylene in recent years. In particular, in the authors' investigation on α,ω-dihexylsexithiophene (DH6T)/P13-based OLETs, the charge transport and light emission demonstrated a close agreement with the recent simulation

Received: January 7, 2019
Revised: April 11, 2019
Published: April 11, 2019

DOI: 10.1021/acs.jpcc.9b00150
J. Phys. Chem. C 2019, 123, 11063−11072

studies performed by Li and Kwok.[27] However, synthesizing materials with high carrier mobility and sufficient photoluminescence (PL) remains limited. Furthermore, efficient charge transport, effective recombination of electrons and holes, and I_{on}/I_{off} are required to be more useful in display applications.[15]

Most of the previous measurements were carried out either under an inert atmosphere or in a vacuum as most organic materials are sensitive to moisture and oxygen that penetrate the channel region.[6−8,13,18,28] Device parameters such as mobilities deteriorate with time, and therefore, the OLETs do not show reproducible device characteristics and operational stability, as shown in the measurements of 2-(4-pentylstyryl) tetracene-based OLETs conducted by Cicoira et al.[29]

In this paper, the fabrication and characterization of multilayered, heterojunction-based OLETs are presented. Pentacene and 4,5-di(9*H*-carbazol-9-yl)phthalonitrile (2CzPN) doped onto 1,3-bis(*N*-carbazolyl)benzene (mCP) were successively deposited as p-type and n-type materials, respectively. In particular, dopant 2CzPN is known as an efficient blue fluorophore.[31] To improve the injection of electrons, Li/Al and TPBi were also used as a low WF electrode and an electron-transport layer, respectively. The molecular structures and relative energy levels (in eV) are displayed in Figure 1. The highest occupied and lowest unoccupied molecular orbitals (HOMOs and LUMOs, respectively) of pentacene, 2CzPN, mCP, and TPBi are estimated to be (−5.0, −2.9), (−5.8, −3.0), (−6.1, −2.4), and (−6.2, −2.7), respectively.[28,31,32] The energy levels are well-matched to inject carriers and form singlet excitons for efficient light emission. The deposition scheme employed herein is the authors' self-made neutral cluster beam deposition (NCBD) apparatus described in detail elsewhere.[6−8,13,18,28,33−35] The unique advantages of the NCBD method in growing films are enhanced packing density, crystallinity, room-temperature deposition, and surface morphology, which cannot be achieved using other vapor deposition and/or solution-processing techniques.

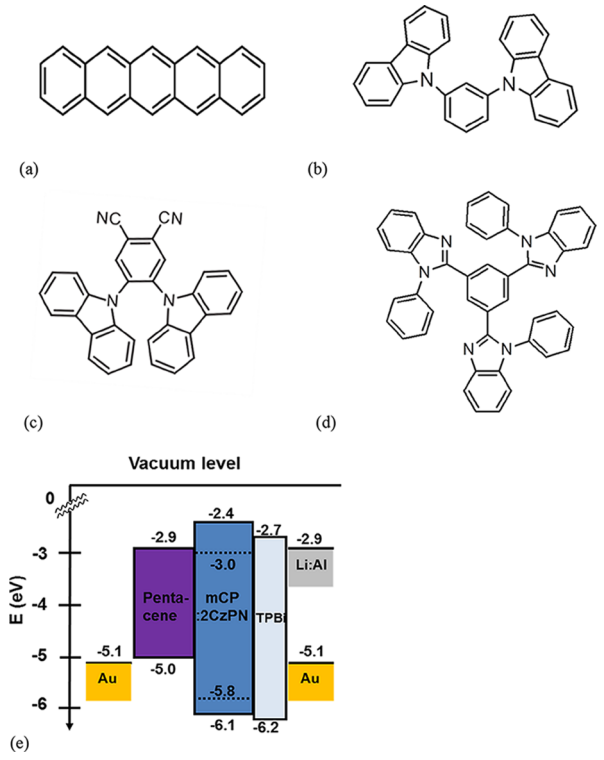

Figure 1. Molecular structures of (a) pentacene, (b) mCP, (c) 2CzPN, and (d) TPBi. (e) Energy-level diagram for Au electrode/pentacene (bottom)/mCP:2CzPN (middle)/TPBi (top)/Au or Li/Al electrode (units in eV).

Herein, focus is first placed upon the morphological, structural, and luminescence characterization of the organic active layers by microscopy, diffraction method, and luminescence spectroscopy. Different device parameters were derived from the current−voltage ($I-V$) and current−voltage−light emission ($I-V-L$) characteristics of the OLETs obtained in air. The heterojunction-based OLETs exhibited acceptable device performance and EL near the drain electrode. The conduction and light emission mechanisms in action for the observed EL are discussed based on the charge-coupled device (CCD) photographic images.

EXPERIMENTAL SECTION

A schematic view of multilayered, heterojunction-based OLETs with a top-contact, long-channel geometry is displayed in Figure 2: bilayered devices with symmetric (Au only) and asymmetric (Au and Li/Al) electrode configurations called devices A and B, and trilayered OLETs with a third TPBi layer with symmetric and asymmetric electrode configurations called devices C and D. The four types of devices were fabricated to clarify the functions of the symmetry of the electrodes and an additional TPBi layer for the $I-V$ and $I-V-L$ characteristics. All OLETs were fabricated using thermally grown SiO_2 (300 nm) on a highly n-doped Si wafer.

All OLETs were fabricated using thermally grown SiO_2 (300 nm) on a highly n-doped Si wafer. SiO_2 and n-doped Si wafer were used as the gate dielectric layer and gate electrode, respectively. A successive cleaning procedure was applied to the SiO_2 gate dielectrics to improve the device performance: ultrasonic cleaning with acetone, hot trichloroethylene, HNO_3 (20%), methanol, deionized water, and then blowing with dry N_2 followed by UV (254 nm) treatment for 15 min.[13]

A layer of 50 nm of pentacene (Sigma-Aldrich Co.) as a hole-transport layer was deposited at an evaporation rate of 0.7−1.0 Å/s in a high vacuum of 6×10^{-6} Torr using a custom-made NCBD apparatus. mCP and 2CzPN (LUMTEC Co.) as electron-transport and emissive dopant layers were co-deposited to a thickness of 50 nm directly on top of the pentacene layer. For devices C and D, 10 nm of TPBi (LUMTEC Co.) as an electron-transport layer was then evaporated on top of the mCP:2CzPN layer. For the source and drain electrodes of symmetric devices A and C, Au was evaporated on top of the mCP:2CzPN layer and TPBi at a deposition rate of 2.5 Å/s with a thickness of 50 nm by a shadow mask. For asymmetric devices B and D, Au and Li/Al were successively deposited at a rate of 2.5 Å/s for the Au electrode with a thickness of 50 nm and at a rate of 3.5 Å/s for the Li/Al electrode with a thickness of 70 nm. The channel length (L) and width (W) of the OLETs were 200 μm and 10 mm, respectively.

The morphology and crystallinity of the thin films grown on the dielectric substrates were scanned utilizing atomic force microscopy (AFM) (PSI Co.) and X-ray diffraction (XRD) (Rigaku Co.). The PL spectra of the thin films were acquired using an F7000 (Hitachi Ltd.) instrument. An optical probe

DOI: 10.1021/acs.jpcc.9b00150
J. Phys. Chem. C 2019, 123, 11063−11072

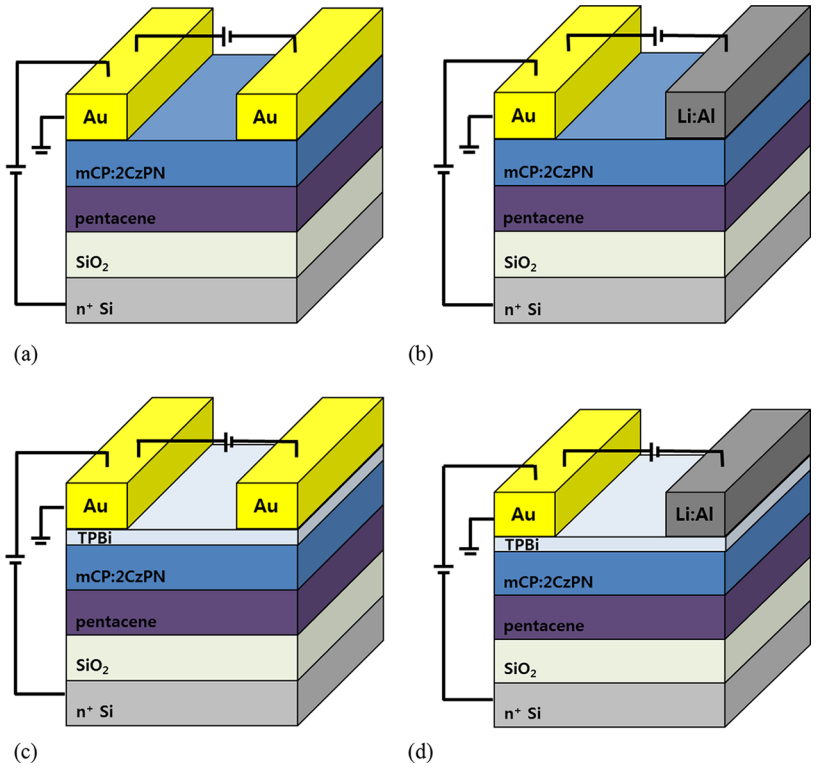

Figure 2. Bi- or trilayered, heterojunction-based OLETs with top-contact geometry: (a) device A, (b) device B, (c) device C, and (d) device D.

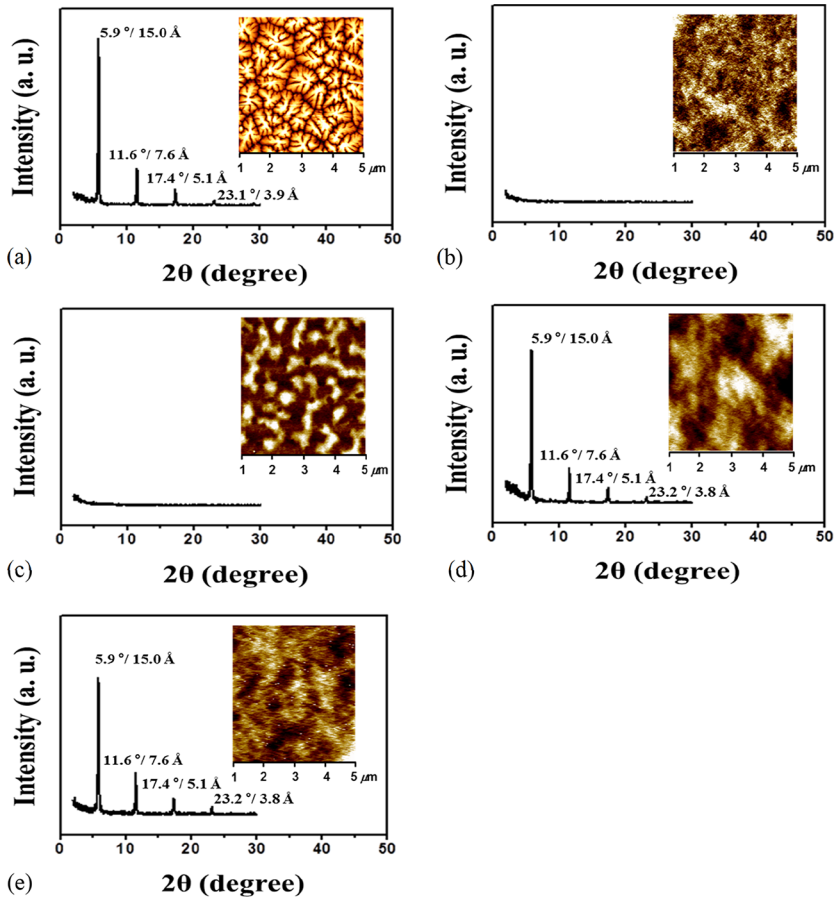

Figure 3. X-ray diffractograms and AFM micrographs (insets: $5 \times 5\ \mu m^2$) for (a) pentacene, (b) mCP:2CzPN, (c) TPBi, (d) pentacene (bottom)/mCP:2CzPN (top), and (e) pentacene (bottom)/mCP:2CzPN (middle)/TPBi (top) thin films deposited on SiO_2 substrates at room temperature.

DOI: 10.1021/acs.jpcc.9b00150
J. Phys. Chem. C 2019, 123, 11063−11072

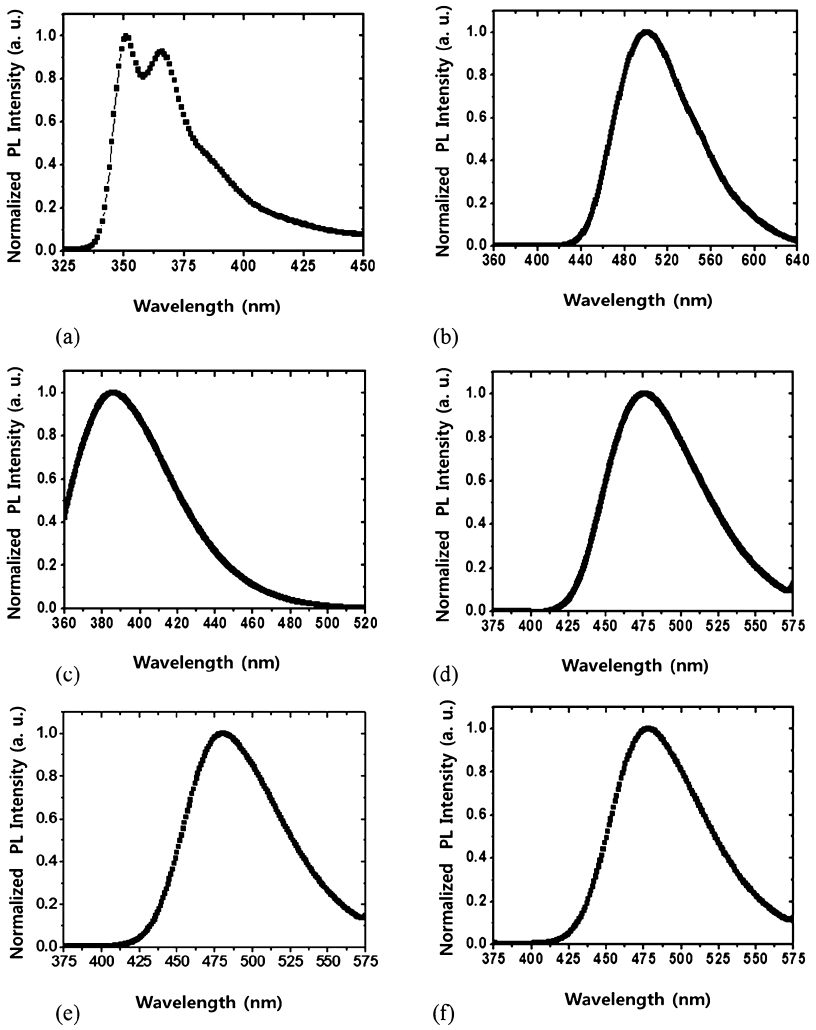

Figure 4. Normalized PL spectra of single-layered (a) mCP, (b) 2CzPN, (c) TPBi, and (d) mCP:2CzPN with the excitation wavelength (λ_{ex}) of 290, 330, 312, and 290 nm. (e) Bilayered pentacene/mCP:2CzPN and (f) trilayered pentacene/mCP:2CzPN/TPBi layers with λ_{ex} of 290 nm.

linked to an HP4145B and an 818-UV Si photodiode equipped with an 1830 C power meter (Newport Co.) were used to obtain the $I-V$ and $I-V-L$ plots of the OLETs in air. The EL photographic images of the OLETs were captured by a CCD camera (Q Imaging Co.) fixed on an optical microscope.

RESULTS AND DISCUSSION

Comparative Analysis of Thin Films. Comparative characterization of the surface morphological and structural properties for different thin films deposited on top of SiO_2 substrates at room temperature was examined using AFM and XRD. The topographic two-dimensional AFM images of the single-layered pentacene (50 nm), mCP:2CzPN (50 nm), TPBi (50 nm), bilayered pentacene (bottom, 50 nm)/mCP:2CzPN (top, 50 nm), and trilayered pentacene (bottom, 50 nm)/mCP:2CzPN (middle, 50 nm)/TPBi (top, 50 nm) films were observed by running section analyses over 5.0 × 5.0 μm^2 in a noncontact mode, as displayed in Figure 3. All five films exhibited pin-hole free, complete coverage, and the average root-mean-square roughness (R_{rms}) values for the pentacene, mCP:2CzPN, TPBi, pentacene/mCP:2CzPN, and trilayered pentacene/mCP:2CzPN/TPBi films were measured to be 6.8, 0.18, 0.91, 0.32, and 0.24 nm, respectively. The observed low R_{rms} values for the films deposited using the NCBD scheme indicated that the weakly bound cluster beams of organic semiconducting molecules undergo efficient fragmentation into energetic individual molecules to form uniform and highly packed films without the requirement for a thermal annealing process.

The XRD diffractograms of the single-layered pentacene (50 nm), mCP:2CzPN (50 nm), TPBi (50 nm), bilayered pentacene (bottom, 50 nm)/mCP:2CzPN (top, 50 nm), and trilayered pentacene (bottom, 50 nm)/mCP:2CzPN (middle, 50 nm)/TPBi (top, 10 nm) films deposited on the SiO_2 substrates in Figure 3 were obtained in a symmetric reflection, coupled ($\theta-2\theta$) mode (0.154 nm Cu Kα radiation). As indicated in Figure 3a, several multiple-order diffraction peaks were observed in the pure pentacene films. The sharp first-order peak and distinct three higher order peaks can be matched to a sequence of (00l) reflection lines with multiple d spacings on the basis of the crystallographic parameters of pentacene: the four reflection peaks located at 5.9°, 11.6°, 17.4°, and 23.1° are equal to 15.0, 7.6, 5.1, and 3.9 Å, which correspond to the highly ordered triclinic pentacene film. In the cases of single-layered mCP:2CzPN and TPBi films grown on SiO_2, as displayed in Figure 3b,c, there were no peaks, indicating that the films were amorphous.[36,37] In the cases of the bi- and trilayered films in Figure 3d,e, the diffractograms

DOI: 10.1021/acs.jpcc.9b00150
J. Phys. Chem. C 2019, 123, 11063−11072

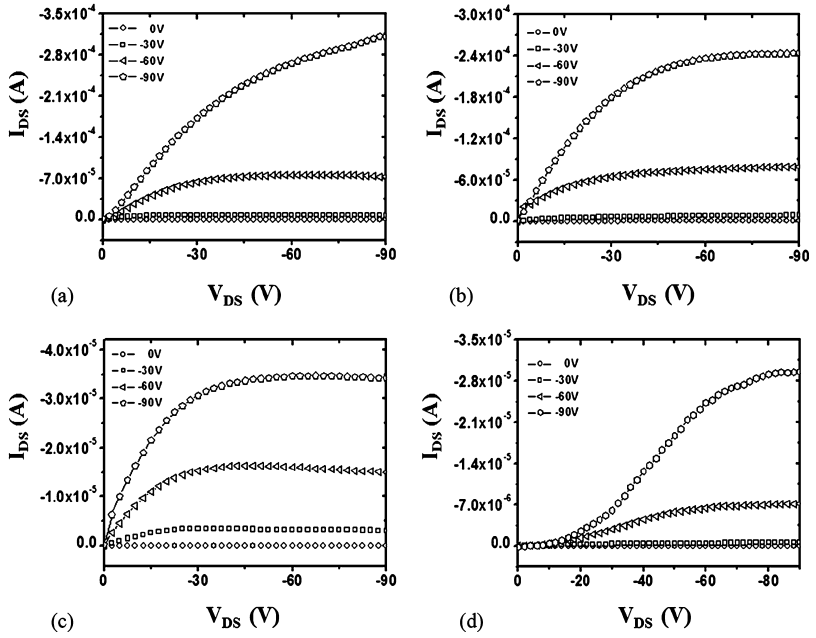

Figure 5. Typical output (drain current I_{DS} vs drain voltage V_{DS}) characteristics of bi- or trilayered, heterojunction-based OLETs: (a) device A, (b) device B, (c) device C, and (d) device D.

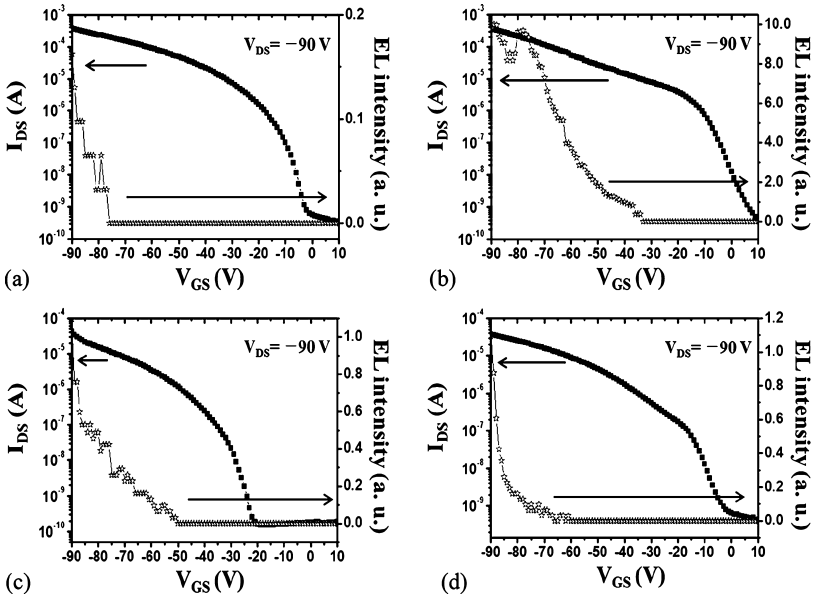

Figure 6. Typical transfer (drain current I_{DS} vs gate voltage V_{GS}) characteristics of bi- or trilayered, heterojunction-based OLETs: (a) device A, (b) device B, (c) device C, (d) device D, and the corresponding EL curves obtained in air.

displayed a simple feature composed of lower signal-to-noise ratio and distinct individual peaks from only the bottom pentacene films. Preparation of smooth, continuous crystalline pentacene films results in favorable hopping of the majority charge carriers between the well-packed grain crystallites, which is essential in devising high-performance, heterojunction-based OLETs.

The PL spectra of the different films were monitored using a laser radiation with an excitation wavelength (λ_{ex}) in the region of 290−330 nm. The typical normalized PL spectra of single-layered films of mCP, 2CzPN, and TPBi are displayed in Figure 4a−c; the PL peaks were located approximately at 351/366, 502, and 385 nm, respectively.[30,38] A pentacene film is known to exhibit no fluorescence in the condensed phase.[17] In the cases of the 2CzPN-doped mCP and multilayered films displayed in Figure 4d−f, only one blue emission peak positioned near 480 nm was observed. Because of the substantial overlap between the PL spectrum of the mCP host and the absorption spectrum of the 2CzPN dopant, an efficient energy transfer from mCP (band gap E_g = 3.7 eV in Figure 1) to 2CzPN (E_g = 2.8 eV) was expected to occur in the co-evaporated or multilayered films. The peak position was reported to be strongly dependent on the 2CzPN dopant concentration, and in this study, the optimized doping concentration of 2CzPN in mCP corresponded to the level of 6 wt % with an emission peak wavelength of ca. 480 nm.[32,39]

Device Parameters from *I*−*V* Characteristics. The effects of drain electrodes (Au or Li/Al) and TPBi on the

DOI: 10.1021/acs.jpcc.9b00150
J. Phys. Chem. C 2019, 123, 11063−11072

Table 1. Comparison of Device Parameters Deduced from the Fits of Observed *I*−*V* and *I*−*V*−*L* Characteristics for Bi- and Trilayered A−D Devices with Corresponding Standard Deviations (σ)

	$\mu_{eff}^{h,avg} \pm \sigma$ (cm^2/V s)	I_{on}/I_{off}	$V_T \pm \sigma$ (V)	$N_{trap} \pm \sigma$ ($\times 10^{12}$ cm^{-2})	$V_{EL\ starting} \pm \sigma$ (V)
device A	0.31 ± 0.063	$6 \times 10^5 \pm 3 \times 10^5$	−33.0 ± 5.0	2.03 ± 0.46	−77.0 ± 6.8
device B	0.25 ± 0.13	$4 \times 10^5 \pm 4 \times 10^5$	−40.6 ± 9.1	2.43 ± 0.37	−33.0 ± 10.2
device C	0.073 ± 0.0065	$2 \times 10^5 \pm 1 \times 10^5$	−56.4 ± 4.8	2.46 ± 0.24	−51.0 ± 4.0
device D	0.067 ± 0.025	$1 \times 10^5 \pm 3 \times 10^4$	−41.7 ± 4.8	2.51 ± 0.59	−61.0 ± 3.6

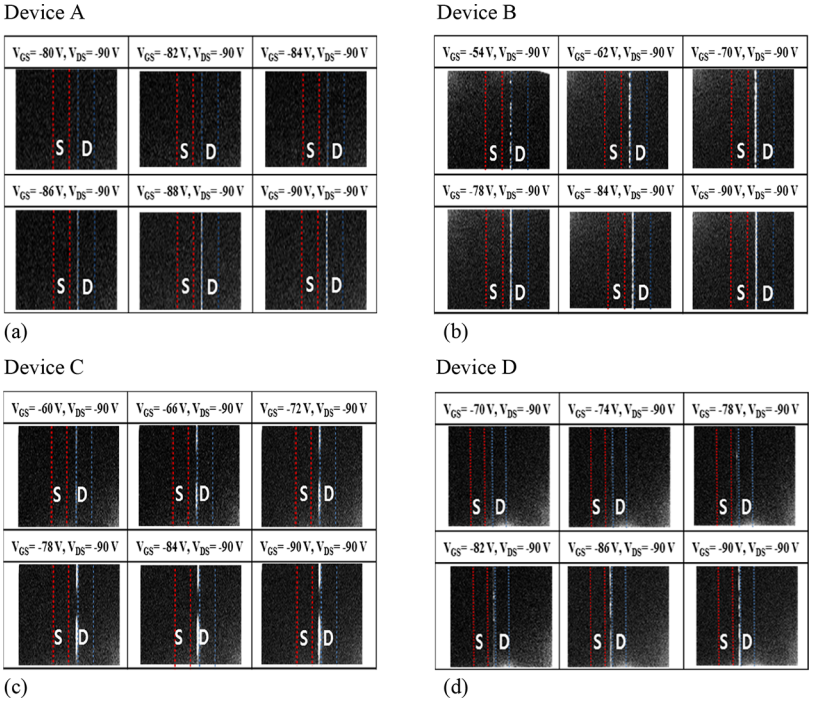

Figure 7. EL images of bi- or trilayered, heterojunction-based OLETs captured with a CCD camera under proper gate and drain biases (exposure time = 2 s). Red and blue lines indicate the source and drain electrodes and are colored to clearly identify the positions of EL emission: (a) device A, (b) device B, (c) device C, and (d) device D. For all OLETs, gradually increasing edge emission occurred only near the electron-injecting electrode, i.e., drain electrode.

device performance were examined under ambient conditions. Figures 5 and 6 display the typical output and transfer characteristics of the multilayered, heterojunction-based transistors A−D with the corresponding EL curves. All the output plots in Figure 5 indicate the dependence of drain current (I_{DS}) on the drain and gate voltages (V_{DS}, V_{GS}) expected for the typical unipolar p-type characteristics functioning in accumulation mode, which consist of linear and saturation regimes. The average field-effect hole mobilities ($\mu_{eff}^{h,avg}$) can be directly deduced from the transfer curves in the saturation regime in Figure 6: each transfer scan was performed at a constant V_{DS}, where I_{DS} satisfies the following relationship

$$I_{DS} = \frac{WC_i\mu_{eff}}{2L}(V_{GS} - V_T)^2$$

where W and L refer to the channel width and length, respectively. C_i and V_T refer to the gate dielectric capacitance per unit area and the threshold voltage, respectively. The C_i value measured for SiO_2 was 11.6 nF/cm^2. Using standard OFET analysis, the values for $\mu_{eff}^{h,avg}$ obtained from the fits of the transfer characteristics for 10 transistors with standard deviation (σ) are listed in Table 1, with the other device parameters I_{on}/I_{off}, V_T, and trap density (N_{trap}).

In Table 1, it is clear that the $\mu_{eff}^{h,avg}$ values of the bilayered A and B OLETs were higher than those of the trilayered C and D OLETs by the order of magnitude of 3 or 4 times. The values of the bilayered transistors were comparable to or somewhat less than those obtained from the single-layered, polycrystalline pentacene-based transistors grown on SiO_2 dielectrics, which were among the best to date.[34] The decrease of the $\mu_{eff}^{h,avg}$ values observed in the trilayered devices appears to be unavoidable. In the present OLET configuration in Figure 2, when the gate electrode is negatively biased for the bottom pentacene layer, the middle mCP:2CzPN (50 nm) and particularly the top TPBi (10 nm) layers in direct contact with the source electrode act as blocking layers with a high energy barrier for hole injection (the HOMO values of mCP and TPBi: −6.1 and −6.2 eV in Figure 1). The resultant unfavorable hole injection and conduction lead to an ineffective hole accumulation at the bottom pentacene layer and could explain why the extent of $\mu_{eff}^{h,avg}$ reduction in the trilayered C and D devices was considerably substantial. Similar behavior was also reported in the studies of multilayered organic devices.[15] Here, although mCP and TPBi are known as ambipolar and n-type semiconductors, the magnitude of the $\mu_{eff}^{e,avg}$ value was measured to be low, corresponding to the space−charge-limited case.[40,41] Therefore, a well-balanced ambipolar carrier transport was not expected in the present heterojunction-based

DOI: 10.1021/acs.jpcc.9b00150
J. Phys. Chem. C 2019, 123, 11063−11072

OLET devices, and the asymmetric electrode configuration could promote the facile injection of electrons, which resulted in substantial EL intensity, as described below.

The high $\mu_{eff}^{h,avg}$ values observed in the bilayered A and B devices were ascribed primarily to the growth of high-quality pentacene layers. As indicated in the aforementioned XRD and AFM results, the authors' NCBD scheme improved the growth of closely packed and nanometer-sized grain crystallites on the SiO_2 dielectrics without any thermal post-treatment. In fact, the favorable improvement was directly revealed in the N_{trap} values. The traps are known to be associated with structural disorders and defects in the active organic layers and therefore strongly correlate with OFET and OLET performance. The N_{trap} value can be determined using the following equation

$$N_{trap} = \frac{C_i|V_T - V_{TO}|}{q}$$

where q is the elementary charge.[42] The values derived for the films of the A–D devices are listed in Table 1. The low N_{trap} values of the whole devices indicate that the pentacene-active layers with high quality experienced good hole conduction. The large pentacene grains were likely to reduce grain boundary-induced scattering during hole conduction, resulting in an acceptable device performance.

***I–V–L* and EL Mechanism.** The EL intensity (I_{EL}) was also recorded during the monitoring of the transfer $I–V$ characteristics. Further, a series of photographic EL images were simultaneously obtained using a CCD camera linked to an optical microscope to analyze I_{EL} and emitting positions more clearly. To increase the light emission, in this study, the efficient blue fluorophore 2CzPN was doped onto the mCP layer. Figures 6 and 7 display the V_{GS} dependence of I_{EL} and CCD images for the A–D devices: the light emission was detected only in the vicinity of the drain electrode in all A–D devices, and there was a tendency for I_{EL} to increase with decreasing V_{GS} (i.e., increasing $|V_{GS}|$) at a fixed V_{DS} = −90 V. In the $I–V–L$ characteristics, the most intense emission was observed in the bilayered B device at V_{GS} < −35 V, whereas the weakest emission was observed in device A at V_{GS} < −75 V; the two trilayered C and D devices demonstrated comparable I_{EL}.

In principle, the emitting position and the dependence of I_{EL} on the gate bias can be explained according to the spatial distributions of hole and electron carriers under proper V_{GS} and the injection barriers depending on the HOMO–LUMO energy levels. I_{EL} is expressed in terms of the general relation $I_{EL} \propto pn\,(\mu_{eff}^{h} + \mu_{eff}^{e})$, where p and n, respectively, refer to the hole and electron carrier densities. In the case of ideal OLETs with balanced p ≈ n, the maximum emission occurs at $V_{GS} = 1/2V_{DS}$, where the same voltage drop exists for the hole and electron carriers. In the majority of multilayered, heterojunction-based OLETs, however, owing to the unbalanced carrier densities (i.e., typically p ≫ n), the relationship cannot be generally fulfilled, and the ordinary shortage of the highly mobile electron carriers significantly results in the dependency of the EL process on the gate biases V_{GS}, as indicated in Figure 6.

A key part for understanding the EL process observed in this study is related to the ease of electron injection, layer structure, and location of hole–electron recombination. Figure 8 presents the schematic energy diagrams of the entire injection, transport, and recombination of charges under different bias

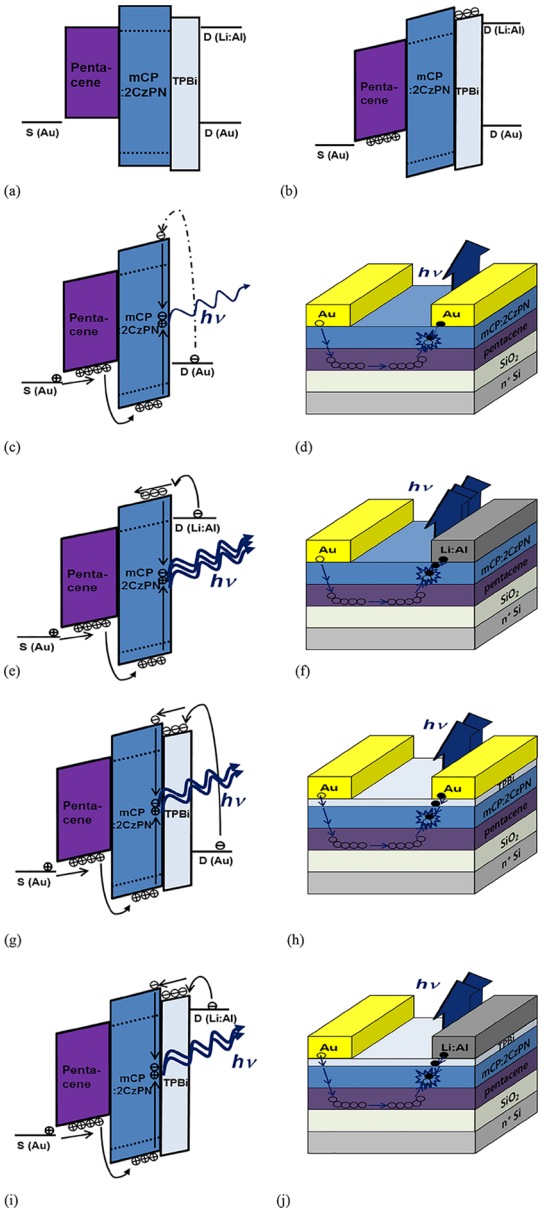

Figure 8. Operating conduction mechanisms of bi- or trilayered heterojunction-based OLETs with the corresponding energy-level diagrams to explain light emission (a) at $V_{GS} = V_{DS} = 0$ V and (b) at $V_{GS} = 0$ V, $V_{DS} < 0$ V. (c,d) Device A, (e,f) device B, (g,h) device C, and (i,j) device D at $V_{GS} < 0$ V, $V_{DS} < 0$ V.

conditions. At a fixed V_{DS} = −90 V, the electric field gradient is formed between the electrodes of the drain and source, as pointed out in Figure 8a,b. As V_{GS} is more negatively biased (i.e., increasing $|V_{GS}|$), the HOMO and LUMO levels of the organic active layers move up with respect to the energy levels of the source and drain electrodes, which causes a decrease in the hole injection barrier and an increase in the electron injection barrier. Then, the holes easily injected from the high-WF Au source electrodes flow into the HOMO level of the pentacene layer, and the accumulation layer forms an active channel for hole carriers in the bottom pentacene layer. Conversely, electrons injected from the drain electrodes are necessary to overcome the unfavorable higher injection barrier to flow into the LUMO levels of mCP:2CzPN in devices A and B or the LUMO levels of the TBBi/mCP:2CzPN layer in

DOI: 10.1021/acs.jpcc.9b00150
J. Phys. Chem. C 2019, 123, 11063–11072

devices C and D. Afterward, at certain $-V_{GS}$ values ($V_{turn\text{-}on}^{EL}$ in Table 1), the recombination of holes and electrons begins to form singlet excitons in the mCP layer followed by Förster energy transfer to the 2CzPN dopants with a smaller band gap, where the resultant light emission occurs. As anticipated in the energy diagram of Figure 1, the characteristic EL emission was due only to the highly fluorescent 2CzPN dopant molecules, which trap electron and hole charge carriers efficiently and accept energy well from the mCP host matrix. The observed EL was consistent with the aforementioned PL spectrum. I_{EL} increased with increasing $|V_{GS}|$, as indicated in the $I-V-L$ characteristics of Figure 6. Here, owing to the high electron injection barrier, the singlet exciton formation and subsequent energy transfer responsible for the substantial EL always occurred near the drain electrode, where the electrons are injected, as clearly displayed in the captured CCD images in Figure 7.

In the cases of bilayered OLETs, I_{EL} was significantly enhanced in the asymmetric device B adopting the low-WF Li/Al drain electrode owing to the lower injection barrier. Although the charge transport was governed by the hole transport in the pentacene layer, more electron injection from the Li/Al electrode formed superior hole−electron density balance. Such facile injection led to higher exciton formation followed by the emission of a more intense EL in the vicinity of the electron-injecting drain electrode of the device B at lower $V_{turn\text{-}on}^{EL} < -35$ V compared to the device A occurring at $V_{turn\text{-}on}^{EL} < -75$ V. In the cases of the trilayered devices, although the widely used TPBi as an electron-transporting layer in OLEDs was inserted to boost the electron transport, the third layer rather induced higher V_T, $V_{turn\text{-}on}^{EL}$, and N_{trap}. As suggested by the lower $\mu_{eff}^{h,avg}$ and I_{on}/I_{off} values, for the devices C and D, the transport and I_{EL} did not increase significantly by tuning the electron injection through high- and low-WF metals.

Several recent OLET systems have demonstrated similar EL phenomena occurring only in the vicinity of the drain electrodes at the proper negative bias.[13,15,16,43] In particular, the present authors' work on P13/ DH6T devices was consistent with the carrier transport and EL predicted by the simulation investigations.[7,27] Conversely, our observation stands in sharp contrast with previous studies of ambipolar devices. For example, in the measurements of thiophene/P13-based ambipolar OLETs conducted by Muccini et al., EL was observed in both the $(\pm)V_{GS}$ region.[23] In the case of DH4T/P13-based OLETs reported by Dinelli and co-workers, the layer in direct contact with the dielectric governed the EL phenomena, irrespective of the deposition sequence of the organic thin films.[44] Understanding the overall EL phenomena from the multilayered OLETs clearly depends on the mobilities of the organic active layers with different HOMO and LUMO energy levels, electrode materials, bias conditions, deposition scheme, and device configuration. Additional combined experimental and theoretical studies are required to develop the comprehensive operating EL mechanisms and the structure−performance relationships. Several optoelectronic devices using different semiconducting organic molecules are in progress.

CONCLUSIONS

Bi- or trilayered, heterojunction-based OLETs with a top-contact geometry were fabricated using the NCBD method. The surface morphology and crystallinity of the organic films were examined by AFM and XRD. Further, different device parameters of the OLETs such as $\mu_{eff}^{h,avg}$, I_{on}/I_{off}, V_T, $V_{turn\text{-}on}^{EL}$, N_{trap}, and I_{EL} were deduced from the fits of the $I-V$ and $I-V-L$ characteristics observed in air. The effects of the drain electrodes (Au or Li/Al) and TPBi on the device performance were also examined under ambient conditions. All devices demonstrated both electrical switching functionality and control of EL in air. In particular, I_{EL} was significantly enhanced in the asymmetric bilayered device adopting the low-WF Li/Al drain electrode owing to the lower electron injection barrier. The trilayered devices utilizing TPBi as an electron-transporting layer rather indicated higher V_T, $V_{turn\text{-}on}^{EL}$, and N_{trap}, and the transport and I_{EL} did not increase significantly by tuning the drain electrodes through high- and low-WF metals. Operating light emission mechanisms responsible for the observed EL and recombination zone were discussed with the aid of photographic images provided by a CCD camera. We hope that the authors' investigation can provide insight into the operating EL mechanism and structure−performance relationships of π-conjugated, organic-based optoelectronic devices at the molecular level.

AUTHOR INFORMATION

Corresponding Author

*E-mail: jhc@korea.ac.kr. Phone: +82 2 3290 3135. Fax: +82 2 3290 3121.

ORCID

Jong-Ho Choi: 0000-0001-6673-200X

Notes

The authors declare no competing financial interest.

ACKNOWLEDGMENTS

This research was supported by the Basic Science Research Program through the National Research Foundation of Korea (NRF) funded by the Ministry of Education (NRF20100020209 and NRF2017R1D1A1B03027893).

REFERENCES

(1) Hepp, A.; Heil, H.; Weise, W.; Ahles, M.; Schmechel, R.; Seggern, H. V. Light-emitting Field-effect Transistor Based on a Tetracene Thin Film. *Phys. Rev. Lett.* **2003**, *91*, 157406.

(2) Muccini, M. Bright Future for Organic Field-Effect Transistors. *Nat. Mater.* **2006**, *5*, 605−613.

(3) Capelli, R.; Toffanin, S.; Generali, G.; Usta, H.; Facchetti, A.; Muccini, M. Organic Light-Emitting Transistors with an Efficiency that Outperforms the Equivalent Light-Emitting Diodes. *Nat. Mater.* **2010**, *9*, 496−503.

(4) Di, C. A.; Yu, G.; Liu, Y. Q.; Xu, X. J.; Wei, D. C.; Song, Y. B.; Sun, Y. M.; Wang, Y.; Zhu, D. B. Organic Light-Emitting Transistors Containing a Laterally Arranged Heterojunction. *Adv. Funct. Mater.* **2007**, *17*, 1567−1573.

(5) Ooi, Z.-E.; Foong, T. R. B.; Singh, S. P.; Leok Chan, K.; Dodabalapur, A. A Light Emitting Transistor Based on a Hybrid Metal Oxide-Organic Semiconductor Lateral Heterostructure. *Appl. Phys. Lett.* **2012**, *100*, 093302.

(6) Kim, D.-K.; Oh, J.-D.; Shin, E.-S.; Seo, H.-S.; Choi, J.-H. Study on Copper Phthalocyanine and Perylene-based Ambipolar Organic Light-Emitting Field-Effect Transistors Produced using Neutral Beam Deposition Method. *J. Appl. Phys.* **2014**, *115*, 164503.

(7) Seo, H.-S.; Zhang, Y.; An, M.-J.; Choi, J.-H. Fabrication and Characterization of Air-Stable, Ambipolar Heterojunction-Based Organic Light-Emitting Field-Effect Transistors. *Org. Electron.* **2009**, *10*, 1293−1299.

DOI: 10.1021/acs.jpcc.9b00150
J. Phys. Chem. C 2019, 123, 11063−11072

(8) Seo, H.-S.; An, M.-J.; Zhang, Y.; Choi, J.-H. Characterization of Perylene and Tetracene-Based Ambipolar Light-Emitting Field-Effect Transistors. *J. Phys. Chem. C* **2010**, *114*, 6141−6147.
(9) Ullah, M.; Tandy, K.; Li, J.; Shi, Z.; Burn, P. L.; Namdas, E. B.; Namdas, E. B. High-Mobility, Heterostructure Light-Emitting Transistors and Complementary Inverters. *ACS Photonics* **2014**, *1*, 954−959.
(10) Maasoumi, F.; Ullah, M.; Shaw, P. E.; Li, J.; Burn, P. L.; Meredith, P.; Namdas, E. B. Charge Transport and Recombination in Heterostructure Organic Light Emitting Transistors. *Org. Electron.* **2015**, *25*, 37−43.
(11) Zaumseil, J.; Friend, R. H.; Sirringhaus, H. Spatial Control of the Recombination Zone in an Ambipolar Light-Emitting Organic Transistor. *Nat. Mater.* **2006**, *5*, 69−74.
(12) Loi, M. A.; Rost-Bietsch, C.; Murgia, M.; Karg, S.; Riess, W.; Muccini, M. Tuning Optoelectronic Properties of Ambipolar Organic Light-Emitting Transistors Using a Bulk-Heterojunction Approach. *Adv. Funct. Mater.* **2006**, *16*, 41−47.
(13) Kim, D.-K.; Oh, J.-D.; Kim, J.-W.; Lee, H.-Y.; Choi, J.-H. Effects of Doping and Electrode Contacts on Performance of Organic Light-Emitting Transistors Based on Pentacene and Tris(8-hydroxyquinoline)aluminum. *J. Phys. Chem. C* **2016**, *120*, 13716−13724.
(14) Tandy, K.; Ullah, M.; Burn, P. L.; Meredith, P.; Namdas, E. B. Unlocking The Full Potential of Light Emitting Field-effect Transistors by Engineering Charge Injection Layers. *Org. Electron.* **2013**, *14*, 2953−2961.
(15) Song, L.; Hu, Y.; Li, D.; Chen, H.; Liu, X. Pixeled Electroluminescence from Multilayer Heterostructure Organic Light-Emitting Transistors. *J. Phys. Chem. C* **2015**, *119*, 20237−20243.
(16) Song, L.; Hu, Y.; Zhang, N.; Li, Y.; Lin, J.; Liu, X. Improved Performance of Organic Light-Emitting Field-Effect Transistors by Interfacial Modification of Hole-Transport Layer/Emission Layer: Incorporating Organic Heterojunctions. *ACS Appl. Mater. Interfaces* **2016**, *8*, 14063−14070.
(17) Dadvand, A.; Moiseev, A. G.; Sawabe, K.; Sun, W.-H.; Djukic, B.; Chung, I.; Takenobu, T.; Rosei, F. Maximizing Field-Effect Mobility and Solid-State Luminescence in Organic Semiconductors. *Angew. Chem., Int. Ed.* **2012**, *51*, 3837−3841.
(18) Perepichka, D.-K.; Choi, J.-H. A Study of Effects of Electrode Contacts on Performance of Organic-based Light-Emitting Field-Effect Transistors. *Opt. Mater.* **2018**, *76*, 359−367.
(19) Rost, C.; Karg, S.; Riess, W.; Loi, M. A.; Murgia, M.; Muccini, M. Light-Emitting Ambipolar Organic Heterostructure Field-Effect Transistor. *Synth. Met.* **2004**, *146*, 237−241.
(20) Züfle, S.; Altazin, S.; Hofmann, A.; Jäger, L.; Neukom, M. T.; Schmidt, T. D.; Brütting, W.; Ruhstaller, B. The Use of Charge Extraction by Linearly Increasing Voltage in Polar Organic Light-emitting Diodes. *J. Appl. Phys.* **2017**, *121*, 175501.
(21) Liu, Z.-Y.; Tseng, S.-R.; Chao, Y.-C.; Chen, C.-Y.; Meng, H.-F.; Horng, S.-F.; Wu, Y.-H.; Chen, S.-H. Solution-Processed Small Molecular Electron Transport Layer for Multilayer Polymer Light-Emitting Diodes. *Synth. Met.* **2011**, *161*, 426−430.
(22) Zaumseil, J.; Donley, C. L.; Kim, J.-S.; Friend, R. H.; Sirringhaus, H. Efficient Top-Gate, Ambipolar, Light-Emitting Field-Effect Transistors Based on a Green-Light-Emitting Polyfluorene. *Adv. Mater.* **2006**, *18*, 2708−2712.
(23) Capelli, R.; Dinelli, F.; Loi, M. A.; Murgia, M.; Zamboni, R.; Muccini, M. Ambipolar Organic Light-Emitting Transistors Employing Heterojunctions of n-Type and p-Type Materials As the Active Layer. *J. Phys.: Condens. Matter* **2006**, *18*, S2127.
(24) Dinelli, F.; Capelli, R.; Loi, M. A.; Murgia, M.; Muccini, M.; Facchetti, A. High-Mobility Ambipolar Transport in Organic Light-Emitting Transistors. *Adv. Mater.* **2006**, *18*, 1416−1420.
(25) Hu, Y.; Lin, J.; Song, L.; Lu, Q.; Zhu, W.; Liu, X. Vertical Microcavity Organic Light Emitting Field-effect Transistors. *Sci. Rep.* **2016**, *6*, 23210.
(26) Hu, Y.; Song, L.; Li, D.; Lin, J.; Liu, X. In-plane Electroluminescence from Microcavity Organic Light-emitting Transistors. *Org. Electron.* **2015**, *26*, 92−98.
(27) Li, W.; Kwok, H. L. Charge Transport and Light Emission in Bilayer Organic Field-Effect Transistors. *Thin Solid Films* **2012**, *520*, 3600−3604.
(28) Seo, H.-S.; Kim, D.-K.; Oh, J.-D.; Shin, E.-S.; Choi, J.-H. Organic Light-Emitting Field-Effect Transistors Based upon Pentacene and Perylene. *J. Phys. Chem. C* **2013**, *117*, 4764−4770.
(29) Cicoira, F.; Santato, C.; Dadvand, A.; Harnagea, C.; Pignolet, A.; Bellutti, P.; Xiang, Z.; Rosei, F.; Meng, H.; Perepichka, D. F. Environmentally Stable Light Emitting Field-Effect Transistors Based on 2-(4-pentylstyryl)tetracene. *J. Mater. Chem.* **2008**, *18*, 158−161.
(30) Sun, J. W.; Kim, K.-H.; Moon, C.-K.; Lee, J.-H.; Kim, J.-J. Highly Efficient Sky-Blue Fluorescent Organic Light Emitting Diode Based on Mixed Cohost System for Thermally Activated Delayed Fluorescence Emitter (2CzPN). *ACS Appl. Mater. Interfaces* **2016**, *8*, 9806−9810.
(31) Lee, J.; Lee, J.-I.; Lee, J. Y.; Chu, H. Y. Enhanced Efficiency and Reduced Roll-Off in Blue and White Phosphorescent Organic Light-Emitting Diodes with a Mixed Host Structure. *Appl. Phys. Lett.* **2009**, *94*, 193305.
(32) Masui, K.; Nakanotani, H.; Adachi, C. Analysis of Exciton Annihilation in High-efficiency Sky-Blue Organic Light-Emitting Diodes with Thermally Activated Delayed Fluorescence. *Org. Electron.* **2013**, *14*, 2721−2726.
(33) Kim, J.-Y.; Kim, E.-S.; Choi, J.-H. Poly[2-(N-carbazolyl)-5-(2-ethylhexyloxy)-1,4-phenylenevinylene/tris(8-hydroxyquinoline) Aluminum Heterojunction Electroluminescent Devices Produced by Cluster Beam Deposition Methods. *J. Appl. Phys.* **2002**, *91*, 1944−1951.
(34) Seo, H.-S.; Jang, Y.-S.; Zhang, Y.; Syed Abthagir, P.; Choi, J.-H. Fabrication and Characterization of Pentacene-based Transistors with a Room-Temperature Mobility of 1.25 cm^2/Vs. *Org. Electron.* **2008**, *9*, 432−438.
(35) Zhang, Y.; Seo, H.-S.; An, M.-J.; Oh, J.-D.; Choi, J.-H. Influence of Gate Dielectrics on The Performance of Single-layered Organic Transistors And Bi-layered Organic Light-emitting Transistors Prepared by the Neutral Cluster Beam Deposition Method. *J. Appl. Phys.* **2011**, *109*, 084503.
(36) Suzuki, F.; Shizu, K.; Kawaguchi, H.; Furukawa, S.; Sato, T.; Tanaka, K.; Kaji, H. Multiscale Simulation of Charge Transport in a Host Material, N,N'-Dicarbazole-3,5-Benzene (mCP), for Organic Light-Emitting Diodes. *J. Mater. Chem. C* **2015**, *3*, 5549−5555.
(37) Yu, X.; Yu, J.; Zhou, J.; Huang, W.; Lin, H. Organic Field-effect Transistors with a Sandwich Structure from Inserting 2,2',2''-(1,3,5-Benzenetriyl)Tris[1-Phenyl-1Hbenzimidazole] in the Pentacene Active Layer. *Eur. Phys. J.: Appl. Phys.* **2013**, *62*, 20101.
(38) Anikeeva, P. O.; Halpert, J. E.; Bawendi, M. G.; Bulović, V. Quantum Dot Light-Emitting Devices with Electroluminescence Tunable over the Entire Visible Spectrum. *Nano Lett.* **2009**, *9*, 2532−2536.
(39) Liu, W.; Zheng, C.-J.; Wang, K.; Zhang, M.; Chen, D.-Y.; Tao, S.-L.; Li, F.; Dong, Y.-P.; Lee, C.-S.; Ou, X.-M.; Zhang, X.-H. High Performance All Fluorescence White Organic Light Emitting Devices with a Highly Simplified Structure Based on Thermally Activated Delayed Fluorescence Dopants and Host. *ACS Appl. Mater. Interfaces* **2016**, *8*, 32984−32991.
(40) Tsuboi, T.; Liu, S.-W.; Wu, M.-F.; Chen, C.-T. Spectroscopic and Electrical Characteristics of Highly Efficient Tetraphenylsilane-carbazole Organic Compound as Host Material for Blue Organic Light Emitting Diodes. *Org. Electron.* **2009**, *10*, 1372−1377.
(41) Lee, H.; Ahn, H.; Lee, C. Device Characteristics of Blue Phosphorescent Organic Light-Emitting Diodes Depending on The Electron Transport Materials. *J. Inf. Disp.* **2011**, *12*, 219−222.
(42) Pernstich, K. P.; Haas, S.; Oberhoff, D.; Goldmann, C.; Gundlach, D. J.; Batlogg, B.; Rashid, A. N.; Schitter, G. Threshold Voltage Shift in Organic Field Effect Transistors by Dipole

DOI: 10.1021/acs.jpcc.9b00150
J. Phys. Chem. C 2019, 123, 11063−11072

Monolayers on The Gate Insulator. *J. Appl. Phys.* **2004**, *96*, 6431−6438.
(43) Cui, S.; Hu, Y.; Lou, Z.; Yi, R.; Hou, Y.; Teng, F. Light Emitting Field-Effect Transistors with Vertical Heterojunctions Based on Pentacene and Tris-(8-hydroxyquinolinato) Aluminum. *Org. Electron.* **2015**, *22*, 51−55.
(44) Dinelli, F.; Capelli, R.; Loi, M. A.; Murgia, M.; Muccini, M.; Facchetti, A.; Marks, T. J. High-Mobility Ambipolar Transport in Organic Light-Emitting Transistors. *Adv. Mater.* **2006**, *18*, 1416−1420.

DOI: 10.1021/acs.jpcc.9b00150
J. Phys. Chem. C 2019, 123, 11063−11072